PNAS RESEARCH ARTICLE | PHYSICS

Dichotomous dynamics of magnetic monopole fluids

Chun-Chih Hsu[a,1], Hiroto Takahashi[a,1], Fabian Jerzembeck[a,b], Jahnatta Dasini[c], Chaia Carroll[c], Ritika Dusad[a], Jonathan Ward[c], Catherine Dawson[c], Sudarshan Sharma[d], Graeme M. Luke[d], Stephen J. Blundell[a], Claudio Castelnovo[e], Jonathan N. Hallén[e,f], Roderich Moessner[f], and J. C. Séamus Davis[a,b,c,g,2]

Contributed by J. C. Séamus Davis; received November 22, 2023; accepted April 17, 2024; reviewed by Collin L. Broholm and Cristiano Nisoli

A recent advance in the study of emergent magnetic monopoles was the discovery that monopole motion is restricted to dynamical fractal trajectories [J. N. Hallén *et al.*, *Science* 378, 1218 (2022)], thus explaining the characteristics of magnetic monopole noise spectra [R. Dusad *et al.*, *Nature* 571, 234 (2019); A. M. Samarakoon *et al.*, *Proc. Natl. Acad. Sci. U.S.A.* 119, e2117453119 (2022)]. Here, we apply this novel theory to explore the dynamics of field-driven monopole currents, finding them composed of two quite distinct transport processes: initially swift fractal rearrangements of local monopole configurations followed by conventional monopole diffusion. This theory also predicts a characteristic frequency dependence of the dissipative loss angle for AC field–driven currents. To explore these novel perspectives on monopole transport, we introduce simultaneous monopole current control and measurement techniques using SQUID-based monopole current sensors. For the canonical material $Dy_2Ti_2O_7$, we measure $\Phi(t)$, the time dependence of magnetic flux threading the sample when a net monopole current $J(t) = \dot{\Phi}(t)/\mu_0$ is generated by applying an external magnetic field $B_0(t)$. These experiments find a sharp dichotomy of monopole currents, separated by their distinct relaxation time constants before and after $t \sim 600$ μs from monopole current initiation. Application of sinusoidal magnetic fields $B_0(t) = B\cos(\omega t)$ generates oscillating monopole currents whose loss angle $\theta(f)$ exhibits a characteristic transition at frequency $f \approx 1.8$ kHz over the same temperature range. Finally, the magnetic noise power is also dichotomic, diminishing sharply after $t \sim 600$ μs. This complex phenomenology represents an unprecedented form of dynamical heterogeneity generated by the interplay of fractionalization and local spin configurational symmetry.

dysprosium titanate | magnetic dynamics | spin ice | frustrated magnetism

Significance

How magnetic monopole currents traverse spin-ice materials has proven notoriously difficult to understand. Recently, it was discovered that emergent dynamical fractal trajectories underpin the monopole motion. Applying these novel concepts to field-driven magnetic monopole currents predicts a characteristic dichotomy in both their DC and AC dynamics. Experimental investigations using monopole current spectroscopy then reveal a strong dichotomy in the monopole current response to applied DC and AC magnetic fields and in monopole noise. An accurate atomic-scale understanding of the mechanisms of magnetic monopole currents in spin ice is thereby established. They are constrained by the geometry of allowed fractal trajectories subject to specific spin-configuration termini to monopole motion. Such self-generated dynamical heterogeneity represents a paradigm in quantum magnetic transport.

The existence of a fluid of emergent magnetic monopoles (1, 2) in pyrochlore spin-ice materials (3) is now well attested (4). However, a comprehensive microscopic understanding of the dynamics of monopole transport currents (5) remains a profound challenge. In such spin-ice compounds (3, 4), e.g., $Dy_2Ti_2O_7$ and $Ho_2Ti_2O_7$, the lowest energy magnetic excitations are emergent magnetic charges (monopoles) (1, 2). Each Dy^{3+} or Ho^{3+} magnetic ion occupies a vertex of the corner-sharing tetrahedral sublattice and exhibits only two magnetic states with dipole moments $\mu \approx 10\ \mu_B$, pointing either toward or away from the center of each tetrahedron (Fig. 1*A*). Moreover, the lowest energy configuration of each tetrahedron is constrained by the dipolar-spin-ice Hamiltonian (6) to have two spins pointing in and two pointing out (2in-2out), while the higher energy excitations are the effective magnetic charges ($+m$ for 3in-1out and $-m$ for 1in-3out) that are in some degree mobile (2). Explaining the unusual magnetization dynamics of both $Dy_2Ti_2O_7$ and $Ho_2Ti_2O_7$ has proven perplexing (7–15) and a complete microscopic transport theory of magnetic monopole currents remains an outstanding challenge. Monte Carlo simulations (16) using the standard model (SM) of spin-ice dynamics (5, 17, 18) as well as theoretical modeling based on random walk theory (18) indicated that thermally activated generation recombination processes and monopole motion give rise to magnetic noise with power spectral density (16, 19), $S(\omega, T) \propto \tau(T)/(1 + (\omega\tau(T))^b)$ versus angular frequency ω, temperature T, and relaxation time τ with b approaching 2. However, when identified (20, 21), the actual magnetic noise exhibited $S_M(\omega, T) \propto \tau(T)/(1 + (\omega\tau(T))^{b(T)})$, whose anomalous noise 'color' with exponent approaching $b(T) = 1.5$ at lowest temperatures represented an outstanding mystery.

Innovative monopole transport theories designed to address this issue now posit that the microscopics of Dy^{3+} spin flips plays a central role in shaping the monopole dynamics. This is adduced to internal transverse magnetic fields being strongly suppressed at Dy^{3+} ion sites for a highly symmetric local spin configuration as shown schematically in the side panels of Fig. 1*A*. In consequence, there are predicted to be two microscopic Dy^{3+} spin-flip rates with

Reviewers: C.L.B., Johns Hopkins University; and C.N., Los Alamos National Laboratory.

The authors declare no competing interest.

[1]C.-C.H. and H.T. contributed equally to this work.

[2]To whom correspondence may be addressed. Email: jcseamusdavis@gmail.com.

This article contains supporting information online at https://www.pnas.org/lookup/suppl/doi:10.1073/pnas.2320384121/-/DCSupplemental.

Published May 14, 2024.

fast and slow time constants (22). Such route-dependent spin-flip restrictions permeate the spin ice crystal and force peripatetic monopoles to traverse a disordered cluster of trajectories whose fractal structure is close to a percolation transition (23). To capture the physics of the two distinct spin-flipping rates, the beyond standard model (bSM) dynamics is simulated by considering the transverse field from the six nearest spins. In particular, monopole hopping occurs on a slow time scale when the spin-flipping transverse field vanishes, and on a fast time scale otherwise. In practice, the slow time scale is expected to be so much longer than the fast one that monopole hopping at this timescale can be neglected (see ref. 23 and *SI Appendix*, section I). The theoretical consequence, supported by bSM Monte Carlo simulations (23) with this bimodal spin-flip constraint, is subdiffusive monopole motion for which $S_M(\omega, T) \propto \tau(T)/(1+(\omega\tau(T))^{b(T)}$ with $b(T) \approx 1.5$. This noise power law is strikingly consistent with the reported experimental magnetic monopole noise spectroscopy results (20, 21).

Analytical and Numerical Monopole Transport Theory

The original research using the bSM theory (23) for monopoles in spin ice focused on magnetic fluctuations and magnetic noise in thermodynamic equilibrium. But this paradigmatic change in understanding also holds profound but unexplored repercussions for monopole current dynamics of these systems when externally driven. Heuristically, we can consider these issues by visualizing a spin-ice sample as shown schematically in Fig. 1*A*. While the monopole drift velocities (v_+, v_-) from oppositely charged monopoles are in opposite directions, the monopole currents ($J_+ \propto mv_+$, $J_- \propto -mv_-$) then occur in the same direction as the applied field B, resulting in a net monopole current $J = J_+ + J_-$. A central ingredient is that the symmetry-derived constraints on spin flips included in the bSM can block monopole motion at local termini, as represented by the monopoles without arrow in Fig. 1*A*. A monopole is considered to be at a terminus if its preferred motion under the influence of the applied field is blocked (*SI Appendix*, section II). The consequences on, and signatures for, nonequilibrium dynamics and such monopole transport theory are entirely unexplored.

To address these issues, here, we consider bSM monopole current dynamics in the two essential cases: a) currents driven by an instantaneous change in the applied magnetic field and b) currents driven by a sinusoidal magnetic field modulation. With a combination of bSM Monte Carlo simulations (*SI Appendix*, section I) and analytical effective modeling (*SI Appendix*, section III) we predict stark dichotomous signatures of bSM monopole current dynamics in these regimes, as illustrated in Fig. 1 *B* and *C*. The pivotal microscopic difference between simple SM and bSM dynamics is the presence of termini in the allowed monopole paths in the latter (Fig. 1*A*), with specific consequences for the monopole current dynamics. In the first case, a step in applied field modifies monopole motion by inducing dichotomous monopole currents that we distinguish as both reconfiguration and polarization currents, respectively. The first involves rapid short-range reconfigurations of the monopoles and reflects both microscopic energetic and dynamical constraints on monopole motion; the second changes the polarization of the system via diffusive monopole motion over larger distances, and it decays on a characteristic timescale τ_P. The reconfiguration current is not present with SM dynamics, and decays on a timescale τ_R (approximately the microscopic fast spin-flip rate τ_{fast}). It can be intuitively pictured as the driven diffusion of monopoles in and out of termini in response to the field. These mechanisms in turn produce a dichotomy of monopole current responses to a sudden change in applied magnetic field: an initial one being a combination of the polarization and the reconfiguration currents and a slower second one related only to the polarization of the system.

An intuitive picture for the dichotomous currents can already be gleaned from a very simple one-dimensional ladder: Imagine a one-dimensional chain along the x direction, each site of which is also connected to two otherwise isolated "termini" sites located diagonally above and below in opposite directions, i.e., in the $\pm(x+y)$ directions (*SI Appendix*, Fig. S3). Consider mobile monopoles on the ladder, subject to a field of magnitude B pointing along the chain, and undergoing incoherent Monte Carlo type dynamics. For a field in the $+x$ direction, negative (positive) monopoles will thus be trapped in the sites above (below) the chain; and, crucially, vice versa for a field in the $-x$ direction. Trapped monopoles must then overcome an energy barrier to escape their termini. Reversing the field will free trapped monopoles on one side of the ladder and instead drive them to the other side of the chain. The concomitant motion of these particles yields the reconfiguration current J_{rec}, which coexists with a steady state current J_{ss}. Explicitly, at small fields $J = J_{ss} + J_{rec} = \frac{B}{3\tau_{fast}T} + \frac{2B}{3\tau_{fast}T} e^{-t/\tau_{fast}}$ (*SI Appendix*, section III). The long decay constant of J_{ss} in spin ice becomes infinite in the absence of a magnetization buildup in the ladder model, while J_{rec} decays with the short time constant which is the charge hopping time, equivalent to the spin-flip time constant τ_{fast} in spin ice. Removing the termini removes the reconfiguration current altogether as occurs equivalently with the dichotomous response in simulations using bSM, but not SM, dynamics. Thus, for example, Fig. 1*B* shows bSM Monte Carlo simulation results for time-dependent magnetization M(t) upon step-wise application of magnetic field of strength 30 mT at time $t = 0$. M_{sat} is the $t \to \infty$ equilibrium value of the magnetization in the presence of the field. The main panel shows results for bSM dynamics at temperatures 1.7, 2.0, 2.4, 3.0, and 4.0 K. Here, the dashed gray lines are exponential fits (highlighting the longer polarization time scale), while the inset contrasts the behavior between bSM and SM dynamics.

In this theory, the response of magnetic monopoles when subject to an oscillating magnetic field should also reflect the dichotomy of polarization and reconfiguration currents. In the limit of small ($f < \tau_R^{-1}, \tau_P^{-1}$) and large ($f > \tau_R^{-1}, \tau_P^{-1}$) driving frequencies, both currents are either in phase or fully out of phase with the driving field. Crucially, however, there is an intermediate range of driving frequencies $\tau_P^{-1} < f < \tau_R^{-1}$, where the polarization and reconfiguration currents are, respectively, out of and in phase with the driving field. This leads to a pronounced feature in the loss angle $\theta(f) = \arctan(\mathrm{Im}J_f/\mathrm{Re}J_f)$ for AC monopole currents $J(f) = \mathrm{Re}J_f + i\mathrm{Im}J_f$ at frequency f. This prediction is visible in Fig. 1*C*, where we show the $\theta(f)$ extracted from Monte Carlo simulations of spin-ice magnetization, $M(t) = M_0 \sin[2\pi ft + \theta(f)]$, in response to an oscillating magnetic field, $B(t) = B_0 \cos(2\pi ft)$, of amplitude $B_0 = 30$ mT applied along the crystal [111] direction. The main figure shows $\theta(f)$ for bSM dynamics at temperatures 0.8, 1.0, 1.3, 1.7, 2.2, 3.0, and 4.0 K. The inset again contrasts the behavior between bSM and SM dynamics. In *SI Appendix*, section III, we show how this result can also be found on the three-legged ladder model introduced above. These unique perspectives and predictions for bSM monopole current dynamics now motivate our experimental studies to detect and quantify any of the dichotomous transport, dissipation, and fluctuation phenomena anticipated.

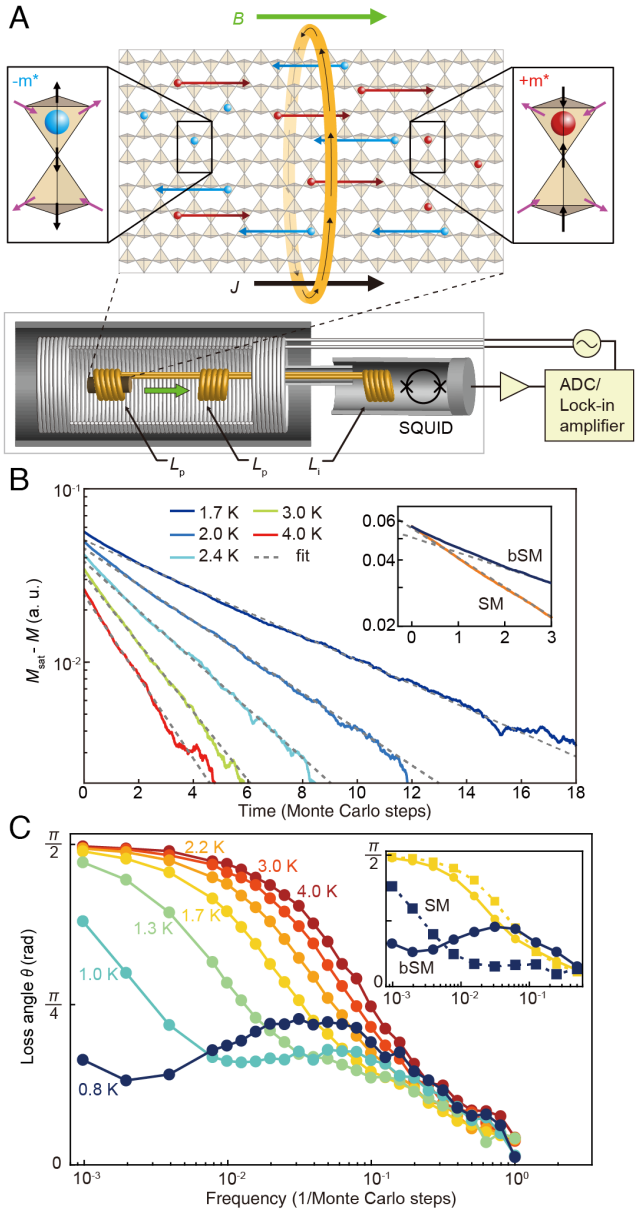

Fig. 1. Simultaneous monopole current control and measurement spectrometer. (*A*) Conceptual representation of magnetic field–driven monopole current $J(t)$ passing through a superconducting loop (yellow). Positive charged monopoles (red) are driven to the right by an applied field B, and negatively charged (blue) to the left. These rapid monopole currents are occasionally terminated when the spin-flip rate is suppressed by specific local spin conformations, magnified within the smaller panels at *Left* and *Right*. *Lower* panel: Conceptual design of simultaneous monopole current control and measurement system based on direct high-precision SQUID sensing of the monopole current $J(t) = (d\Phi/dt)/\mu_0$. (*B*) Monte Carlo simulation results of the magnetic response when an external magnetic field of strength 30 mT is suddenly applied at time $t = 0$. M_{sat} is the equilibrium value of the magnetization in the presence of the field. The main panel shows results for bSM dynamics at temperatures 1.7 K, 2.0 K, 2.4 K, 3.0 K, and 4.0 K (from upper to lower lines). The dashed gray lines are exponential fits (highlighting the longer polarization time scale). The *Inset* contrasts the behavior at shorter times and temperature 1.7 K between bSM (dark blue) and SM (orange) dynamics and the corresponding dashed line fit (highlighting the shorter polarization time scale in SM dynamics). The fast and slow contributions are plotted separately in *SI Appendix*, Fig. S19. (*C*) The loss angle $\theta(f)$ extracted from Monte Carlo simulations of spin-ice magnetization, $m(t) = m_0 \sin[2\pi ft + \theta(f)]$, in response to an oscillating magnetic field, $B(t) = B_0 \cos(2\pi ft)$, of amplitude $B_0 = 30$ mT and frequency f applied along the [111] direction. The main figure shows the loss angle for bSM dynamics at temperatures 0.8 (dark blue), 1.0, 1.3, 1.7, 2.2, 3.0, and 4.0 (dark red) K. A bump-like feature is clearly evident at low temperatures, induced by a reconfiguration current contribution originating from the presence of termini in the emergent dynamical fractal, as explained in the main text. The *Inset* shows the loss angle at 0.8 K (dark blue) and 1.7 K (yellow) for both bSM (circles and solid lines) and SM (squares and dotted lines) dynamics; notice the absence of the characteristic loss-angle feature in the latter.

Simultaneous Monopole Current Control and Spectrometer

The search for such phenomena requires magnetic field–driven monopole currents passing through the pickup coil of a SQUID as shown schematically in Fig. 1*A*. In this situation, $\dot{N}_+$ is the rate of positively charged monopoles (red Fig. 1*A*) driven along the B-field through the loop to the right, and $\dot{N}_-$ the rate of negatively charged monopoles (blue Fig. 1*A*) driven oppositely. Thus, the net monopole current $J(t)$ through the persistent superconducting ring and the associated rate of change of flux $\dot{\Phi}(t)$ threading that ring are

$$J(t) = m\dot{N}_+ - (-m)\dot{N}_- = \dot{\Phi}(t)/\mu_0, \qquad [1]$$

because $\pm m \equiv \pm \Phi_m/\mu_0$ with Φ_m the total magnetic flux of each monopole. To maintain the strict flux quantization required by any persistent superconductive circuit, a spontaneous electrical supercurrent then appears flowing around the ring opposing the flux generated by the monopole current, and it is this supercurrent that is linked inductively to the input coil of a SQUID (*Lower* panel of Fig. 1*A*). To achieve such simultaneous monopole current control and high-precision measurement is technically quite challenging, both because the monopole drive field $B(t)$ applies a giant unwanted flux to the sensing coil and because the whole assembly including the superconductive solenoid generating $B(t)$ must achieve a measurement flux-noise level $\delta\Phi \lesssim 10^{-5}\ \phi_0/\sqrt{\text{Hz}}$ or equivalent field-noise level $\delta B \lesssim 10^{-14}\ \text{T}/\sqrt{\text{Hz}}$. Fig. 1*A* shows a schematic of the system we have developed to meet these specifications (*SI Appendix*, Fig. S10). A continuous superconductive circuit consisting of a pair of opposite chirality pickup coils (L_p in Fig. 1*A*) is assembled along the axis of the drive solenoid (white in Fig. 1*A*) symmetrically about its center point, and connected to the input coil of the SQUID (L_i in Fig. 1*A*). Under these circumstances the applied magnetic field $B(t)$ threads virtually no net flux to the SQUID (*SI Appendix*, Fig. S10). However, if a $Dy_2Ti_2O_7$ sample is introduced to one of the opposite chirality coils (yellow Fig. 1*A*), any monopole currents $J(t)$ driven by $B(t)$ along the axis of that crystal generates a changing flux $\dot{\Phi}(t)$ from Eq. **1**, that can be measured with microsecond precision at the SQUID. The output voltage of the SQUID $V_S(t)$ is related to the flux $\Phi_p(t)$ threading the pickup coil as $\Phi_S(t) = (\mathcal{M}_i/(2L_p + L_i))\Phi_p(t)$; L_p is the sample pickup coil inductance, L_i is the total SQUID-input coil inductance, and $\mathcal{M}_i$ is a mutual inductance to SQUID and

$$V_S(t) = \gamma\Phi_S(t), \qquad [2]$$

where γ is the total gain of the electronics (*SI Appendix*, section IV). Hence, both DC and AC monopole currents $J(t)$ can be generated along the $Dy_2Ti_2O_7$ crystal axis by application of $B(t)$ (green Fig. 2*A*), measured simultaneously with microsecond precision using $\mu_0\Phi_S(t) \propto \int J(t)dt$ (blue Fig. 2*A*), as well as the instantaneous power spectral density of magnetic noise $S_M(\omega, T) \propto S_{\Phi_S}(\omega, T) = \gamma^2 S_{V_S}(\omega, T)$, where $S_{V_S}(\omega, T)$ is the output voltage noise spectrum of the SQUID. Our objective is then to use this spectrometer to search for the dichotomous monopole transport, dissipation, and fluctuation phenomena.

Monopole Current Timescale Dichotomy

$Dy_2Ti_2O_7$ crystals prepared and evaluated for this purpose are inserted into one of the counter wound pickup coils with its long axis along the crystal [351] direction (yellow Fig. 1*A* and *SI Appendix*, section V)

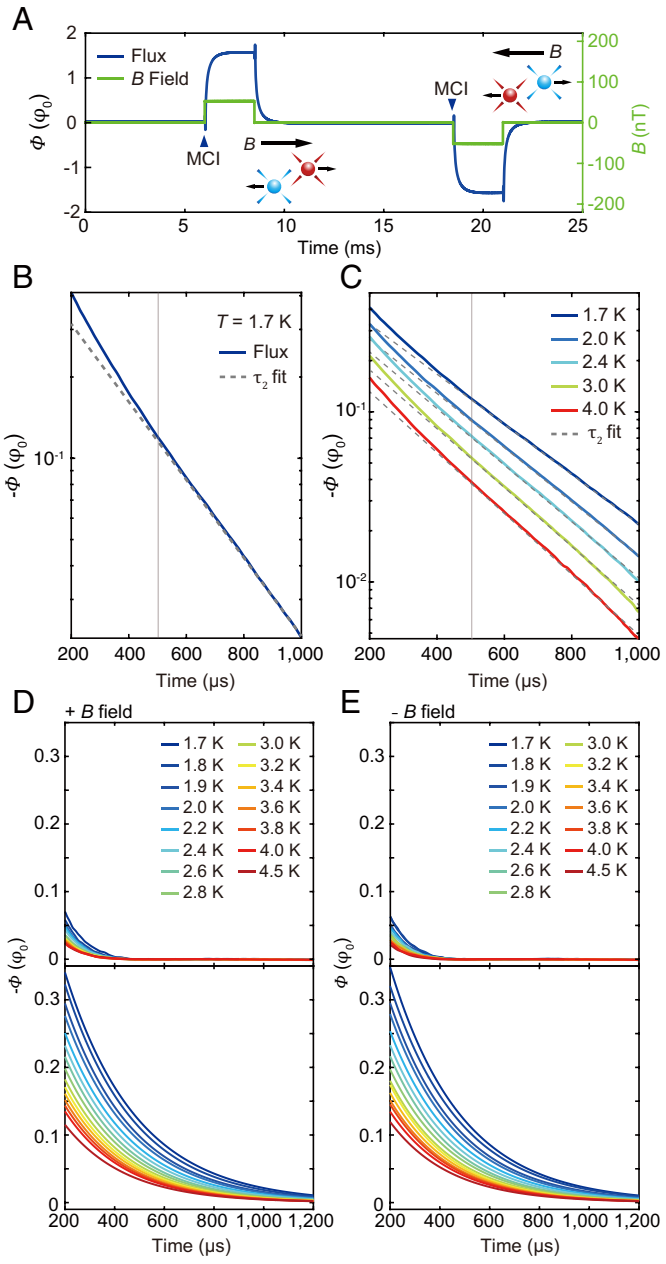

Fig. 2. Magnetic monopole current dichotomy in $Dy_2Ti_2O_7$. (*A*) Typical example of monopole current control generation and detection system in operation. The green trace shows the magnetic field as a function of time while the blue curve is the time dependence of flux $\Phi_S(t)$ measured at the SQUID. Monopole current initiation (MCI) time marked by the blue sign is set to 0 for each current transient. (*B*) Typical example of $\log\Phi_S(t)$ evolution beginning 200 μs after MCI at $t = 0$. Since monopole current is $J(t) = (d\Phi/dt)/\mu_0$ and $\Phi(t) \propto \Phi_S(t)$, these unprocessed data reveal two distinct monopole current regimes. At long times, there is a well-defined time constant τ_2 for monopole current flow as indicated by the dashed straight line fit. At short times $t < 600$ μs from MCI, a transition occurs to a much shorter time constant τ_1 for monopole current flow. (*C*) Measured $\log\Phi_S(t)$ evolution beginning 200 μs after MCI for all temperatures studied and for both positive and negative magnetic field directions. For all transients at long times the time constant $\tau_2(T)$ is measured by a straight line fit. At short times $t < 600$ μs after MCI for all these transients, a transition occurs to a faster time constant $\tau_1(T)$ for monopole current decay. (*D*) Extracted $\Phi_1(t)$ for fast-decaying currents and positive B-field direction. These fast-decaying currents have ceased for $t > 600$ μs from MCI. Simultaneous data in the lower panel show extracted $\Phi_2(t)$ for slow-decaying currents and positive *B*-field direction. (*E*) Extracted $\Phi_1(t)$ for fast-decaying currents and negative *B*-field direction. These fast-decaying currents have ceased for $t > 600$ μs from MCI. Simultaneous data in the lower panel show extracted $\Phi_2(t)$ for slow-decaying currents and negative *B*-field direction. The phenomenology is indistinguishable from that in *D*.

and cooled on board a custom built ultralow vibration refrigerator mounted on the isolated floor-slab of an ultralow vibration laboratory (*SI Appendix*, section IV). Fig. 2*A* shows a typical example of a monopole current control generation and detection experiment. The green trace shows the magnetic field $B(t)$ as a function of time while the blue curve is the time dependence of flux $\Phi_S(t)$ at the SQUID. Axially, there are two possible field $B_{\pm}(t)$ and current $\dot{\Phi}_{S\pm}(t)$ directions here, and both are studied throughout. A typical example of measured $\log\Phi_S(t)$ evolution beginning 200 μs after monopole current initiation (MCI) is shown in Fig. 2*B*. These unprocessed data reveal two distinct monopole current regimes. At long times $t > 600$ μs, we observe a well-defined time constant τ_2 for monopole current flow as indicated by the dashed straight line fit to $\log\Phi_S(t)$. At short times $t < 600$ μs from MCI, a transition occurs to a shorter time constant τ_1 for monopole current flow. To analyze all such curves at all temperatures we fit $\log\Phi_S(t, T) = C(T) - t/\tau_2(T)$ for times 600 μs $< t <$ 1,200 μs and derive $\tau_2(T)$ and $C(T)$ for all examples with fit quality factor $R^2 > 0.99$ (*SI Appendix*, section VI and Fig. S12). The slow-decaying monopole current $\Phi_2(t, T)$ data represented by these fits are subtracted in the time range 200 μs $< t <$ 1,200 μs from the measured $\Phi_S(t, T)$ to yield the residual fast-decaying monopole current $\Phi_1(t, T)$ data, such that $\Phi_S = \Phi_1 + \Phi_2$. Fig. 2 *D*, *Upper* panel shows the resulting $\Phi_1(t, T)$ for fast-decaying currents while the simultaneous $\Phi_2(t, T)$ for slow-decaying currents are shown in the lower panel, both for positive *B*-field direction. Fig. 2*E* shows the equivalent analyzed monopole current data for negative *B*-field direction. In both cases, the fast-decaying monopole currents have ceased for $t > 600$ μs from MCI, while the slow-decaying monopole currents persist for many milliseconds.

Monopole Dissipative Loss Angle and Noise Dichotomy

To probe the possible presence of this dichotomy also in the alternating magnetic monopole current (AC) transport characteristics, we study sinusoidal monopole current generation and detection, a typical example of which is shown in Fig. 3*A*. The green trace shows the applied magnetic field $B_0(t) = B\cos(2\pi ft)$ as a function of time while the blue curve is the simultaneously measured time dependence of flux $\Phi_S(t)$ at the SQUID. AC monopole currents are studied for $10 \leq f \leq 5{,}000$ Hz (*SI Appendix*, section VII). The monopole current $J(t) = \mathrm{Re}J_f\cos(2\pi ft) + i\mathrm{Im}J_f\sin(2\pi ft)$ is determined by using a lock-in amplifier to measure $\Phi_S(t) = \mathrm{Re}\Phi_S\cos(2\pi ft) + i\mathrm{Im}\Phi_S\sin(2\pi ft)$ for all f. The measured flux is linked to the monopole current as $\mathrm{Re}J_f \propto -2\pi f\,\mathrm{Im}\Phi_f$ and $\mathrm{Im}J_f \propto 2\pi f\,\mathrm{Re}\Phi_f$. The measured $\mathrm{Re}J_f$ and $\mathrm{Im}J_f$ for all measured temperatures are shown in Fig. 3*B*. As with any harmonic, charged, non-momentum-conserving fluid dynamics, the dissipation characteristics are established using the loss angle $\theta_d(f) \equiv \arctan(\mathrm{Im}J_f/\mathrm{Re}J_f)$. In Fig. 3*C*, we show measured $\theta_d(f)$ for AC monopole currents in $Dy_2Ti_2O_7$ from all temperatures studied, while the inset shows the frequency f_d associated with a change in the frequency dependence of $\theta_d(f)$. By estimating the frequency f_d which leads to the local maximum in $d\theta_d/df$, AC time constant τ_d is illustrated in Fig. 4*A*, showing a consistent transition at frequency $f_d \cong 1.8$kHz for all temperatures studied.

Finally, we search for a change in the magnetic noise intensity that one might anticipate to occur when the fast-decaying reconfiguration currents have ceased (23). The flux noise intensity

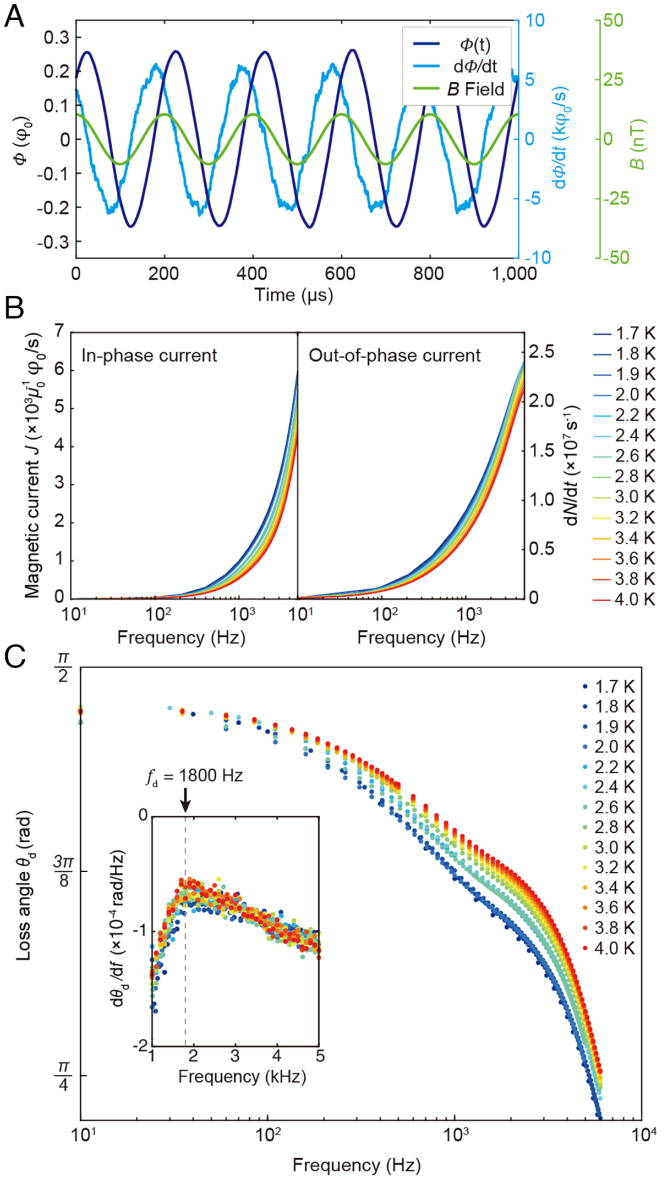

Fig. 3. AC magnetic monopole loss angle in $Dy_2Ti_2O_7$. (*A*) Typical example of sinusoidal monopole current generation and detection. The green trace shows the magnetic field $B_0(t) = B\cos(2\pi ft)$ as a function of time while the dark blue curve is the measured time dependence of flux $\Phi_S(t)$ at the SQUID and the light blue curve is $d\Phi_S(t)/dt$. This field modulation experiment is carried out for 10 Hz $\leq f \leq$ 5,000 Hz. (*B*) From *A* and with $J(t) \propto (d\Phi_S(t)/dt)/\mu_0$, monopole current $J(t) = ReJ_f\cos(2\pi ft) + iImJ_f\sin(2\pi ft)$ is determined by using a lock-in amplifier to measure $\Phi_S(t) = Re\Phi_f\cos(2\pi ft) + iIm\Phi_f\sin(2\pi ft)$ for all f. The consequent in-phase current $ReJ_f \equiv -(2\pi fIm\Phi_f)/\mu_0$ and out-of-phase current $ImJ_f \equiv (2\pi fRe\Phi_f)/\mu_0$ are shown for all temperatures measured. The corresponding rate $\dot{N}$ of the number of monopoles passing through the superconducting loop is estimated by $\dot{N} = \dot{\Phi}_S(t)/\mu_0 m$. The practical rate $\dot{\Phi}_p$ can be converted through the coefficient $M_i/(2L_p + L_i)$. (*C*) Measured $\theta_d(f) = \arctan(ImJ_f/ReJ_f)$ from all temperatures studied. The *Inset* shows that a dissipation transition occurs at $f_d \cong$ 1.8 kHz.

$\sigma_1^2(t) = \langle \Phi_S(t)^2 \rangle$ is measured as soon after MCI as possible thus during the epoch of fast-decaying currents $0 < t < 600$ μs. Subsequently, $\sigma_2^2(t) = \langle \Phi_S(t)^2 \rangle$ is measured throughout the epoch of slow-decaying polarization currents 600 μs $< t <$ 2,000 μs Their ratio σ_1^2/σ_2^2 is shown in Fig. 4*B* exhibiting a constant value near 1.5 for all temperatures (*SI Appendix*, section VIII). The increase of the monopole noise in the reconfiguration current regime is also observed in time dependence of variance (*SI Appendix*, Fig. S13).

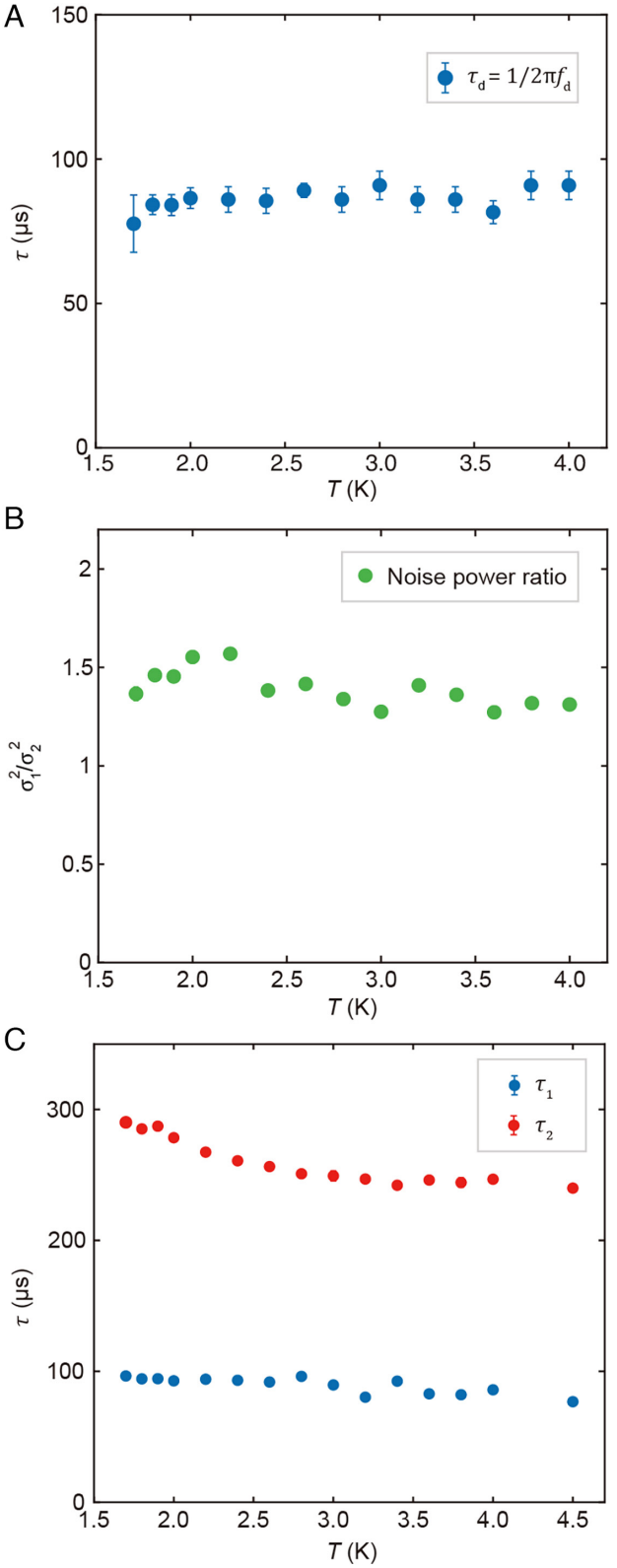

Fig. 4. Dichotomous monopole currents, dissipation, and noise. (*A*) The transition point $\tau_d = 1/2\pi f_d$ where the dissipative process alteration occurs at $f_d \approx$ 1.8 kHz from all temperatures studied. (*B*) Ratio of monopole current–driven magnetization noise intensity σ_1^2 for fast-decaying currents $t <$ 600 μs from MCI to magnetization noise intensity σ_2^2 for slow-decaying currents during 600 μs $< t <$ 1,200 μs. This ratio is constant near 1.5 for all temperatures. (*C*) Experimentally determined monopole current relaxation time constants from all temperatures studied and both field application directions. Measured slow-decaying monopole current time constant τ_2 in solid red; fast-decaying monopole current time constant τ_1 in solid blue.

Hence, the magnetic noise power does indeed drop steeply when the fast-decaying currents disappear at $t \approx 600$ μs.

Discussion

The preeminent feature of these experimental findings is the presence of two distinct timescales (Figs. 2*C* and 4*C*). This is naturally accounted for by the different decay times within the bSM monopole dynamics theory of polarization and reconfiguration currents as in Fig. 1 *B* and *C* (*SI Appendix*, sections I and IX), implying the time scales τ_1 and τ_2 measured in experiments relate directly to the theoretically predicted τ_R and τ_P, respectively. Indeed, this agreement between the bSM monopole current theory and experiments exists in considerable detail: The ratio of the two timescales in both Monte Carlo simulation and experiment hovers around a value of $\frac{\tau_1}{\tau_2} \approx \frac{1}{3}$ in the high-temperature window above 2 K (*SI Appendix*, section X). The values differ by approximately 1/3 in the high-temperature part of our measurement regime, but τ_2 grows significantly faster upon lowering of the temperature in MC simulations than observed in experiments. Neither the monopole density at high temperature (*SI Appendix*, section XI) nor the demagnetization factor from the sample geometry (*SI Appendix*, section XII) could give rise to this observation. The origin of this theoretical discrepancy remains to be understood and is further discussed in *SI Appendix*, section XIII. A characteristic feature in the experimentally measured loss-angle $\theta_d(f, T)$ appears at frequencies $\tau_2^{-1} \lesssim f < \tau_1^{-1}$, as predicted theoretically (Fig. 3*C*), although the phenomenon is discernible at higher temperature than observable by bSM Monte Carlo simulations in Fig. 1*C*. Finally, the magnetic noise power drops steeply after time $t \approx 600$ μs (Fig. 4*B*), indicating suppression of noise once the reconfiguration currents have decayed away on the short timescale τ_1. Thus, the dichotomous monopole transport theory is highly consistent with the observed monopole current phenomenology. Moreover, if there are multiple microscopic spin-flip time constants (23) potentially subtending all dynamical processes in spin ice (24, 25), the dichotomous monopole current theory presented here is quantitatively consistent with the phenomenology of $Dy_2Ti_2O_7$ for a fast time constant of approximately 90 μs.

To summarize, the recent discovery of dynamical fractal trajectories underpinning equilibrium monopole motion in real materials (23) motivated development of our theory for magnetic monopole currents in spin ice. Using a combination of analytical effective theory and bSM Monte Carlo simulations, this theory predicts a dichotomy of the driven monopole current dynamics with characteristic signatures in measurable quantities. State-of-the-art monopole current spectroscopy developed to explore these predictions identifies strong dichotomy in the monopole current response of $Dy_2Ti_2O_7$ to sudden changes in applied magnetic fields, and in the dissipative loss-angle in response to AC fields, as well as in the magnetization noise. The consequence is an accurately predictive, atomic-scale mechanism for magnetic monopole currents in spin ice. Uniquely, as in the case of equilibrium fractal dynamics, this involves the geometry of allowed trajectories subject to energetic and dynamical constraints, in particular the termini to monopole motion. This new paradigm is of self-generated dynamical heterogeneities in quantum magnetic transport which are not caused solely by energetic constraints (e.g., interactions), nor by geometric constraints (e.g., excluded volume effects), nor by quenched disorder. Instead, we demonstrate how the interplay of atomic-scale spin configurations maintaining lattice symmetry nevertheless leads to a distribution of dynamical time scales within an otherwise perfectly crystalline material. Ultimately, this mechanism reveals a broad avenue for identification and exploration of self-constrained dynamics and quantum transport mechanisms in other classes of quantum magnets.

Data, Materials, and Software Availability. CSV files data have been deposited in Zenodo (https://doi.org/10.5281/zenodo.10938856) (26).

ACKNOWLEDGMENTS. We acknowledge and thank E.-A. Kim, S. A. Kivelson, A. P. Mackenzie, and S. Sondhi for key discussions and guidance. J.C.S.D. acknowledges support from the Moore Foundation's EPiQS Initiative through Grant GBMF9457. C.-C.H. and J.C.S.D. acknowledge support from the European Research Council (ERC) under Award DLV-788932. H.T. and J.C.S.D. acknowledge support from the Royal Society under Award R64897. J.C.S.D. and F.J. thank the MPI-CPFS for support. J.D., C. Carroll, J.W., C.D., and J.C.S.D. acknowledge support from the Science Foundation of Ireland under Award SFI 17/RP/5445. C. Carroll acknowledges support from the Irish Research Council under Award GOIPG/2023/4014. G.L. acknowledges support from the Natural Sciences and Engineering Research Council (Canada). S.J.B. acknowledges support from UK Research and Innovation (UKRI) under the UK government's Horizon Europe funding guarantee (Grant No. EP/X025861/1). C. Castelnovo acknowledges support in part from the Engineering and Physical Sciences Research Council (EPSRC) grants No. EP/P034616/1, EP/V062654/1, and EP/T028580/1. J.N.H. and R.M. acknowledge support in part from the Deutsche Forschungsgemeinschaft under grants SFB 1143 (project-id 247310070) and the cluster of excellence ct.qmat (EXC 2147, project-id 390858490).

Author affiliations: [a]Clarendon Laboratory, Oxford University, Oxford OX1 3PU, United Kingdom; [b]Max-Planck Institute for Chemical Physics of Solids, Dresden D-01187, Germany; [c]Department of Physics, University College Cork, Cork T12 R5C, Ireland; [d]Department of Physics, McMaster University, Hamilton, ON L8S 4L8, Canada; [e]Theory of Condensed Matter Group, Cavendish Laboratory, University of Cambridge, Cambridge CB3 0HE, United Kingdom; [f]Max Planck Institute for the Physics of Complex Systems, Dresden 01187, Germany; and [g]Department of Physics, Cornell University, Ithaca, NY 14853

Author contributions: R.D., C. Castelnovo, R.M., and J.C.S.D. designed research; C.-C.H. and H.T. performed research; J.D., C. Carroll, J.W., C.D., S.S., and G.M.L. contributed new reagents/analytic tools; C.-C.H., H.T., F.J., and C.D. analyzed data; S.J.B. provided theoretical guidance; C. Castelnovo, J.N.H. and R.M. developed theory and interpretation; and C.-C.H., H.T., F.J., S.J.B., C. Castelnovo, J.N.H., R.M., and J.C.S.D. wrote the paper.

1. C. Castelnovo, R. Moessner, S. L. Sondhi, Magnetic monopoles in spin-ice. *Nature* **451**, 42–45 (2008).
2. C. Castelnovo, R. Moessner, S. L. Sondhi, Spin-ice, fractionalization, and topological order. *Annu. Rev. Condens. Matter Phys.* **3**, 35–55 (2012).
3. S. T. Bramwell, M. J. Gingras, Spin ice state in frustrated magnetic pyrochlore materials. *Science* **294**, 1495–1501 (2001).
4. M. Udagawa, L. Jaubert, *Spin Ice* (Springer, 2021).
5. I. A. Ryzhkin, Magnetic relaxation in rare-earth oxide pyrochlores. *J. Exp. Theor. Phys.* **101**, 481–486 (2005).
6. B. C. den Hertog, M. J. P. Gingras, Dipolar interactions and origin of spin ice in ising pyrochlore magnets. *Phys. Rev. Lett.* **84**, 3430–3433 (2000).
7. K. Matsuhira *et al.*, Spin dynamics at very low temperature in spin ice $Dy_2Ti_2O_7$. *J. Phys. Soc. Jpn* **80**, 123711 (2011).
8. D. Pomaranski *et al.*, Absence of Pauling's residual entropy in thermally equilibrated $Dy_2Ti_2O_7$. *Nat. Phys.* **9**, 353–356 (2013).
9. J. A. Quilliam, I. R. Yaraskavitch, H. A. Dabkowska, B. D. Gaulin, J. B. Kycia, Dynamics of the magnetic susceptibility deep in the Coulomb phase of the dipolar spin ice material $Ho_2Ti_2O_7$. *Phys. Rev. B* **83**, 094424 (2011).
10. L. R. Yaraskavitch *et al.*, Spin dynamics in the frozen state of the dipolar spin ice material $Dy_2Ti_2O_7$. *Phys. Rev. B* **85**, 020410 (2012).
11. H. M. Revell *et al.*, Evidence of impurity and boundary effects on magnetic monopole dynamics in spin ice. *Nat. Phys.* **9**, 34–37 (2012).
12. E. R. Kassner *et al.*, Supercooled spin liquid state in the frustrated pyrochlore $Dy_2Ti_2O_7$. *Proc. Natl. Acad. Sci. U.S.A.* **112**, 8549 (2015).
13. C. Paulsen *et al.*, Far-from-equilibrium monopole dynamics in spin ice. *Nat. Phys.* **10**, 135–139 (2014).
14. M. J. Jackson *et al.*, Dynamic behavior of magnetic avalanches in the spin-ice compound $Dy_2Ti_2O_7$. *Phys. Rev. B* **90**, 064427 (2014).
15. C. Paulsen *et al.*, Nuclear spin assisted quantum tunnelling of magnetic monopoles in spin ice. *Nat. Commun.* **10**, 1509 (2019).

16. F. K. K. Kirschner, F. Flicker, A. Yacoby, N. Y. Yao, S. J. Blundell, Proposal for the detection of magnetic monopoles in spin-ice via nanoscale magnetometry. *Phys. Rev. B* **97**, 140402 (2018).
17. L. D. C. Jaubert, P. C. W. Holdsworth, Signature of magnetic monopole and Dirac string dynamics in spin ice. *Nat. Phys.* **5**, 258–261 (2009).
18. L. D. C. Jaubert, P. C. W. Holdsworth, Magnetic monopole dynamics in spin ice. *J. Phys. Condens. Matter* **23**, 164222 (2011).
19. C. Nisoli, The color of magnetic monopole noise. *Europhys. Lett.* **135**, 57002 (2021).
20. R. Dusad *et al.*, Magnetic monopole noise. *Nature* **571**, 234–239 (2019).
21. A. M. Samarakoon *et al.*, Anomalous magnetic noise in an imperfectly flat landscape in the topological magnet $Dy_2Ti_2O_7$. *Proc. Natl. Acad. Sci. U.S.A.* **119**, e2117453119 (2022).
22. B. Tomasello, C. Castelnovo, R. Moessner, J. Quintanilla, Correlated quantum tunneling of monopoles in spin ice. *Phys. Rev. Lett.* **123**, 067204 (2019).
23. J. N. Hallén, S. A. Grigera, D. A. Tennant, C. Castelnovo, R. Moessner, Dynamical fractal and anomalous noise in a clean magnetic crystal. *Science* **378**, 1218–1221 (2022).
24. S. R. Dunsiger *et al.*, Spin ice: Magnetic excitations without monopole signatures using μ SR. *Phys. Rev. Lett.* **107**, 207207 (2011).
25. Y. Wang *et al.*, Monopolar and dipolar relaxation in spin ice $Ho_2Ti_2O_7$. *Sci. Adv.* **7**, eabg0908 (2021).
26. C.-C. Hsu *et al.*, Dichotomous dynamics of magnetic monopole fluids. Zenodo. https://doi.org/10.5281/zenodo.10938856. Deposited 10 April 2024.